Nuclear Instruments and Methods in Physics Research B 268 (2010) 3295–3305

Contents lists available at ScienceDirect

Nuclear Instruments and Methods in Physics Research B

journal homepage: www.elsevier.com/locate/nimb

Optimization of GEANT4 settings for Proton Pencil Beam Scanning simulations using GATE

Loïc Grevillot [a,b,c,f,*], Thibault Frisson [a,b,c], Nabil Zahra [a,d,c], Damien Bertrand [f], Frédéric Stichelbaut [f], Nicolas Freud [a,e], David Sarrut [a,b,c]

[a] Université de Lyon, F-69622 Lyon, France
[b] Creatis, CNRS UMR 5220, F-69622 Villeurbanne, France
[c] Centre de Lutte Contre le Cancer Léon Bérard, F-69373 Lyon, France
[d] IPNL, CNRS UMR 5822, F-69622 Villeurbanne, France
[e] CNDRI, INSA-Lyon, F-69621 Villeurbanne Cedex, France
[f] IBA, B-1348 Louvain-la-Neuve, Belgium

ARTICLE INFO

Article history:
Received 3 May 2010
Received in revised form 16 July 2010
Available online 5 August 2010

Keywords:
Monte Carlo
GATE
GEANT4
MCNPX
PHITS
Proton
Pencil beam
Active scanning
Spot
Range
TPS benchmarking
Dose distribution
Profiles
Radiochromic films
Bragg-peak

ABSTRACT

This study reports the investigation of different GEANT4 settings for proton therapy applications in the context of Treatment Planning System comparisons. The GEANT4.9.2 release was used through the GATE platform. We focused on the Pencil Beam Scanning delivery technique, which allows for intensity modulated proton therapy applications. The most relevant options and parameters (range cut, step size, database binning) for the simulation that influence the dose deposition were investigated, in order to determine a robust, accurate and efficient simulation environment. In this perspective, simulations of depth-dose profiles and transverse profiles at different depths and energies between 100 and 230 MeV have been assessed against reference measurements in water and PMMA. These measurements were performed in Essen, Germany, with the IBA dedicated Pencil Beam Scanning system, using Bragg-peak chambers and radiochromic films. GEANT4 simulations were also compared to the PHITS.2.14 and MCNPX.2.5.0 Monte Carlo codes. Depth-dose simulations reached 0.3 mm range accuracy compared to NIST CSDA ranges, with a dose agreement of about 1% over a set of five different energies. The transverse profiles simulated using the different Monte Carlo codes showed discrepancies, with up to 15% difference in beam widening between GEANT4 and MCNPX in water. A 8% difference between the GEANT4 multiple scattering and single scattering algorithms was observed. The simulations showed the inability of reproducing the measured transverse dose spreading with depth in PMMA, corroborating the fact that GEANT4 underestimates the lateral dose spreading. GATE was found to be a very convenient simulation environment to perform this study. A reference physics-list and an optimized parameters-list have been proposed. Satisfactory agreement against depth-dose profiles measurements was obtained. The simulation of transverse profiles using different Monte Carlo codes showed significant deviations. This point is crucial for Pencil Beam Scanning delivery simulations and suggests that the GEANT4 multiple scattering algorithm should be revised.

1. Introduction

The main advantage of using ions over photons in radiation therapy is due to their inverse depth-dose profiles, allowing higher doses to tumors, while better sparing healthy tissues. Currently, the most attractive and advanced technique in hadron-therapy consists in irradiating patients with a small pencil beam of a few millimeters in diameter. The pencil beam is scanned transversally in the patient using scanning magnets, while in the longitudinal direction several iso-energy layers are used to cover the whole tumor volume. Paul Scherrer Institute (PSI) in Switzerland for proton therapy and Helmholtzzentrum für Schwerionenforschung (GSI) in Germany for carbon-ion therapy used for the first time an active beam scanning system in 1997 [1].

When computing dose distributions with ions, one critical point is the Bragg-peak range uncertainty. Moreover, for active beam scanning technique, the lateral spreading of each single pencil beam also needs to be correctly accounted for. In this setting, Monte Carlo (MC) simulations became increasingly important for evaluating treatment plans and dose distributions in patients. The dose accuracy reached with analytical algorithms

* Corresponding author at: Université de Lyon, F-69622 Lyon, France.
E-mail address: loic.grevillot@gmail.com (L. Grevillot).

0168-583X/$ - see front matter © 2010 Elsevier B.V. All rights reserved.
doi:10.1016/j.nimb.2010.07.011

implemented in Treatment Planning Systems (TPS) is limited, for instance near heterogeneities. Therefore, MC simulations can be considered as a powerful Quality Assurance (QA) tool. MC has been extensively used at the Massachusetts General Hospital in Boston for TPS comparisons, mostly for passive scattering irradiation techniques, using the GEANT4 toolkit [2]. MC simulations allow for a better understanding of the dose deposition mechanisms in the patient and open many research areas.

In this study, we used GEANT4 version 9.2 through the GATE simulation environment [3]. This study was conducted in order to analyze the physics implemented in GEANT4 and to select the appropriate settings for patient dose calculation, with an ultimate objective of treatment planning benchmarking [2,4]. This work dedicated to proton therapy applications builds upon a previous study oriented toward carbon-ion simulations using older GEANT4 releases [5]. Firstly, a short review of the relevant physics models and parameters available in GEANT4 is presented in Section 2. Secondly, the influence of different settings on dose calculation is investigated in Section 3. A reference physics-list and an optimized parameters-list are proposed afterwards. Comparisons with two other MC codes: MCNPX2.5.0 [6] and PHITS2.14 [7] are presented in Section 4. Experimental measurements in water and PMMA are described and compared to GEANT4 simulations in Sections 5 and 6.

2. Simulation settings

2.1. Pencil beam model

In this study, a simple pencil beam model was used in order to reproduce the nozzle output beam based on reference measurements. The energetic spectrum was assumed Gaussian and adjusted over depth-dose measurements, as presented in Section 6.1. The 2D probability density function (PDF) of protons was considered normal (Gaussian distribution) and adjusted over transverse profile measurements performed at the isocenter (Section 6.2). By convention, Cartesian coordinates were used, with z the beam direction, x and y the lateral directions. In this paper, the expression "spot size" will refer to the PDF parameters σ_x and σ_y: the standard deviation in the x- and y-directions at the isocenter. The role of the beam divergence on the lateral dose spreading in water was estimated to be negligible compared to the effect of multiple Coulomb scattering. This assumption has been proven by simulating a realistic beam divergence of $\sigma = 3$ mrad. Thus, the intrinsic beam divergence was neglected.

2.2. Physics-list selection

For medical physics applications the electromagnetic (EM) standard package with the Option 3 (Opt3) parameters-list is recommended by the GEANT4 Electromagnetic Standard working group [8]. Opt3 refers to options/processes which are described in the next sections and recommends reference parameters to reach a high level of accuracy. Our physics-list is mainly based on a reference paper dedicated to proton therapy applications [9], using the standard package for EM interactions and a recently implemented process (G4UHadronElasticProcess) combined with the G4HadronElastic model for elastic hadronic (HAD) interactions. Details about available models have been discussed elsewhere [9–12]. The only difference in our physics-list compared to the one proposed in [9], is the choice of the inelastic HAD model. By comparing the Bertini, binary cascade, precompound and QMD models against depth-dose measurements in water, the precompound model was found to best match the measurements. No significant difference between the different models was observed for the transverse dose profile Full Width at Half Maximum (FWHM). Therefore, the precompound model was selected for the rest of the study. The satisfactory agreement obtained with the precompound model has been pointed out in two recent studies investigating a model of a proton magnetic beam scanning delivery nozzle [14] and the prompt-gamma production during proton irradiation [15].

2.3. Multiple scattering (MS) and single scattering (SS)

Charged particles while transported through matter are scattered by electromagnetic fields which are produced by the nucleus and orbiting electrons encountered. The simulation of each single interaction (SS algorithm) increases significantly the number of steps and simulation time, but is considered as the reference, since it is based on cross-section measurements. It is shown in Section 4 that SS increases the simulation time by a factor of 10^3. To overcome this issue, condensed algorithms (MS theories) have been developed in order to simulate the mean effect of numerous collisions (SS algorithm) at the end of each step. This mean effect encloses the net displacement, energy loss and change of direction [13]. MS algorithms are considered as exact if they reproduce the SS behavior. Most of the MC codes implemented the MS theories of Molière, Goudsmit-Saunderson or Lewis [13]. Besides the angular distribution after a step, the advantage of the Lewis theory over the others is the computation of the moment of the spatial distribution as well [13]. The computation of the spatial displacement is not part of those theories and each MC code has to incorporate its own algorithm. MS theories are subjects of interest and recent investigations on the scattering power, considered as a key quantity for beam transport in matter, may improve the accuracy of the MS algorithms implemented in MC codes [16,17]. It was shown that the MS algorithm implemented in GEANT4 release 9.1 depends on the step size [17]. Improvements of the scattering power calculation may avoid this dependence in the future. The management of geometrical boundaries is also a complex task, because particles are not allowed to cross a boundary without performing a step. In GEANT4, several *stepping algorithms* [13], which are included in the MS model can be selected: "simple", "safety" and "distanceToBoundary", depending on the accuracy required. The MS model implemented in GEANT4 is based on the Lewis theory and is detailed in [13].

2.4. Relationship between simulation parameters

The two main parameters in a GEANT4 simulation are the *step*, which corresponds to the distance to the next interaction, and the *range cut*, which corresponds to the production threshold for secondary particles (gammas, electrons and positrons) after EM interactions.

The energy loss of ions in matter is governed by EM and HAD processes. Below the range cut threshold, the energy loss occurs continuously along the ion track (at each step), while above the threshold, it is caused by the explicit production of secondary particles (discrete component) [12,13]. All the particles generated are then tracked until no energy is left (see [13] for implementation details). The range of charged particles can be calculated in the Continuous-Slowing-Down Approximation (CSDA range) by integrating the reciprocal of the total stopping power (collision plus nuclear) with respect to energy [18]. The complexity of the stopping power calculation has been detailed in [19]. The continuous energy loss of charged particles is calculated by the restricted stopping power equation, defined in GEANT4 as the Bethe-Bloch formula integrated between 0 and the range cut value [13].

Before starting a simulation, GEANT4 initializes tables to describe EM processes: *lambda* (mean free path), $\frac{dE}{dx}$ (restricted stopping power), *range* and *inverse range tables* [12]. These tables are

pre-calculated according to the simulation parameters defined by the user, in order to save time during the simulation. By default, 84 bins are stored between 100 eV and 100 TeV, corresponding to a resolution of 7 bins/decade for each material, but the *binning* parameter can be adjusted by the user. In fact, the lambda table should be called cross-section (σ) table, because it stores the cross-sections and indirectly indicates the mean free path (λ) values via Eq. (1):

$$\lambda(Z,E) = \frac{1}{n_{at} \times \sigma(Z,E)} \tag{1}$$

where n_{at} is the number of atoms per unit volume, Z is the target atomic number and E *is* the incident particle energy. Range and inverse range tables show the correspondence between range cut and energy. The step length is sampled at each step using the lambda table for EM processes and directly in the database for the HAD processes. Hence, a sufficient number of bins in the different tables is mandatory to accurately describe EM interactions. In the GEANT4 Opt3 parameters-list, 220 bins between 100 eV and 10 TeV, i.e 20 bins/decade, are advised. It is important to note that the range cut threshold influences the values stored in both the lambda and $\frac{dE}{dx}$ tables. Hence, the step lengths sampled, continuous energy loss along the steps and δ_{e^-} production of charged particles depend on the range cut threshold.

2.5. Dealing with the continuous energy loss

The continuous energy loss imposes a limit on the step length, because of the energy dependence of the cross-sections [13]. It is assumed in many MC codes that the cross-section is constant during a step and the continuous energy loss is computed via Eq. (2) [20]:

$$\text{Continuous Energy Loss} = \text{Steplength} \times \frac{dE}{dx} \tag{2}$$

with $\frac{dE}{dx}$ the restricted stopping power of the charged particle at the beginning of the step. In high-gradient cross-section regions, the approximation of constant cross-sections along the step may lead to an inaccurate dose deposit. This point is very significant in hadron-therapy in the Bragg-peak region. The step length can be limited by two user-defined limits: *maximum allowed step* [20] and *stepping function* [12]. The maximum allowed step is managed like a process in competition with the other processes and limits the maximum step length according to a user-given value. The stepping function described in Eq. (3) is a dynamic step limitation which decreases the particle step limit (ΔS_{lim}) parallel to the particle decreasing range (Fig. 1). The stepping function is defined by two parameters: "dRoverRange" and "finalRange". The "dRoverRange" (α_R) parameter defines the maximum step size allowed as a $\frac{\text{step}}{\text{range}}$ ratio. As the particle travels, the maximum step allowed decreases until the particle range (R) becomes lower than the "finalRange" (ρ_R) parameter.

$$\Delta S_{lim} = \alpha_R \cdot R + \rho_R \cdot (1-\alpha_R)\left(2 - \frac{\rho_R}{R}\right) \tag{3}$$

Instead of limiting the step, one can also integrate the mean cross-section and the mean energy loss along the step, so that Eq. (2) becomes Eq. (4)

$$\text{Continuous Energy Loss} = \int^{\text{steplength}} \frac{dE}{dx} dx \tag{4}$$

This solution enables to sample the exact cross-section and mean energy loss via a MC technique [12]. This function is used when the $\frac{E_{loss}}{E}$ ratio is larger than the user-defined *linear loss limit* [20], with E_{loss} and E the particle continuous energy loss and particle kinetic energy. A low threshold can lead to a significant calculation time increase, respectively. Differences between GEANT4.9.2 default options and Opt3 are summarized in Table 1.

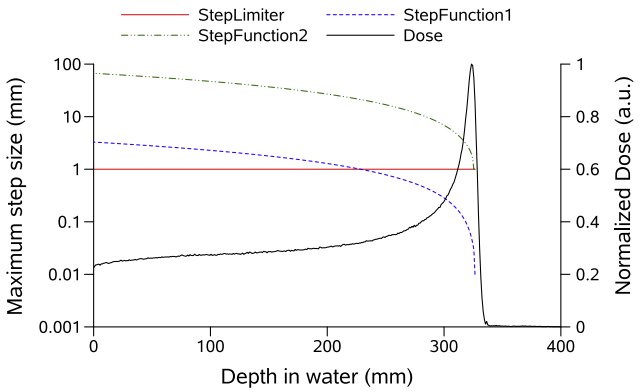

Fig. 1. This figure shows the maximum step length allowed for a 230 MeV proton beam in water, with the stepping function and default parameter ($\alpha_R = 0.2$ and $\rho_R = 1$ mm) in green (StepFunction2); with the stepping function and $\alpha_R = 0.01$ and $\rho_R = 10\,\mu m$ in blue (StepFunction1); with a 1 mm maximum allowed step in red (StepLimiter). The left scale corresponds to the step limit and the right scale corresponds to the normalized dose of the proton beam in black (dose). (For interpretation of the references to colour in this figure legend, the reader is referred to the web version of this article.)

3. Influence of GEANT4 parameters on dose computing

The first objective of our study was to understand the influence of the different parameters and functions presented in Table 1 on proton dose simulation, with a focus on the proton range, the simulation time and the dose fluctuations. For all simulations, the geometry was a single volume of water. Proton ranges were defined as the position of 80% of the maximum dose in the distal fall-off region of the Bragg peak. We evaluated the simulation times by comparing the proton source rate (in protons s^{-1}) for different configurations.

3.1. Influence of the range cut and maximum allowed step values

A 230 MeV mono-energetic proton beam was simulated in a $60 \times 60 \times 60$ cm^3 water tank and the depth-dose profiles were integrated along the z-axis with a 1 mm step. For a 230 MeV proton beam, the NIST [18] CSDA range is 329.4 mm, while the GEANT4 ranges vary from 329.4 mm for a 1 μm range cut to 334.9 mm for a 0.1 mm range cut without fixed step limitation. Results are depicted in Fig. 2. Simulations were performed for different range cut values between 1 μm and 1 mm, using different maximum allowed step values, while other parameters were set to default values.

The proton range converges towards the NIST range when the range cut value decreases. This is observed without step limitation, but introducing such a constraint brings more consistency in the convergence. Indeed, since the step size is related to the range cut value, the range convergence observed for decreasing range cut values is in fact indirectly due to step size limitation. The relationship between the two parameters has been checked by varying the maximum allowed step for different range cut values.

Not surprisingly, the increased accuracy at a very low range cut yields a significant simulation time increase, as also reported in [5] for carbon ions. The simulation time increase is also related to the step size limitation associated with decreasing range cut value. Consequently, both the proton range and the computation time are strongly related to the step size, while the similar effects observed with low range cut values are mainly due to the step short-

Table 1
Summary of the GEANT4.9.2 default and Opt3 parameters.

	e^-/e^+	Proton	GenericIon
	Default values		
Range cut	1 mm	–	–
Stepping function – finalRange	1 mm	1 mm	0.1 mm
Stepping function – dRoverRange	0.2	0.2	0.1
Binning (bins/decade)	7	7	7
Linear loss limit	0.01	0.01	0.15
Stepping algorithm	Safety	Minimal	Minimal
	GEANT4 Opt3		
Stepping function – finalRange	0.1 mm	0.05 mm	0.02 mm
Binning (bins/decade)	20	20	20
Stepping algorithm	DistanceToBoundary	–	–

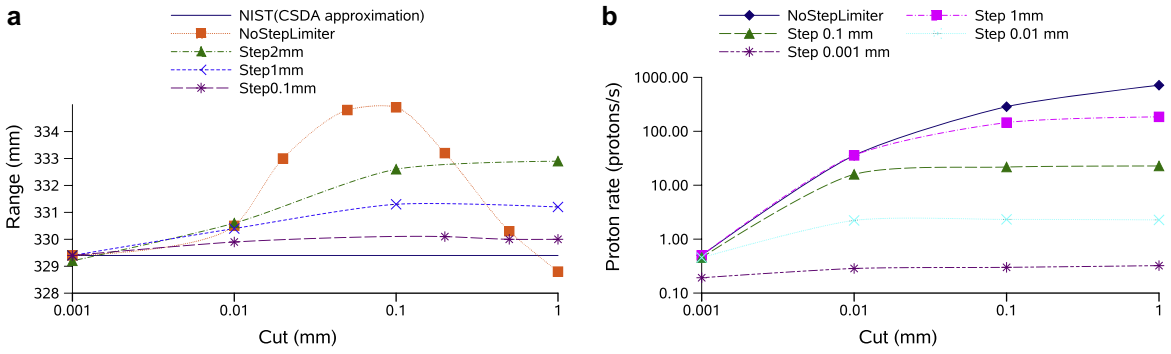

Fig. 2. This figure illustrates the influence of the range cut value on the range of 230 MeV protons in water (a) and simulation time (b) for different maximum allowed step values. Ranges converge to the NIST reference value for sufficiently low range cut and step. Low range cut and step values decrease the proton rate drastically.

ening effect. Part of the time increase is also due to the electron tracking process, which increases with low range cut values.

The influence of the range cut and hence indirectly of the step limitation on dose computing artifacts is presented in Fig. 3. No fixed step limitation was used. When the range cut is sufficiently low, fluctuations become negligible. The worst case occurs with a range cut value of 0.1 mm (highest fluctuations and range shift). Ideally, the range cut value should neither affect the proton range, nor the dose fluctuations. In theory, the electron range cut should only define the accuracy of the electronic dose distribution in the medium.

3.2. Influence of the pre-calculated table binning

In a second stage, the influence of the binning parameter on the dose deposition for several simulations initialized between 7 and 50 bins/decade was examined. We set the binning energy range between 100 eV and 1 GeV to decrease the total number of bins. The range cut was set to 0.1 mm, without limiting the step, which was the worst case observed previously (Section 3.1). Dose calculation deviations were evaluated using Eq. (5)

$$\epsilon = \frac{1}{N}\sum_{i=1}^{N}\left(\frac{|d_i - d_{ref_i}|}{d_{ref_i}}\right) \tag{5}$$

where ϵ is the mean point-to-point deviation calculated, i corresponds to a given curve point, N is the number of points in a curve, d_i is the dose computed and d_{ref_i} is the dose computed for the reference simulation. Deviations were calculated between 0 and the Bragg-peak range (ϵ_{80}) to discard Bragg-peak tail deviations.

The influence of EM table binning on dose computing is presented in Fig. 4 (a) and (b). Fluctuations decreased as the number of bins per decade increased. Based on this result, the 50 bins/dec-

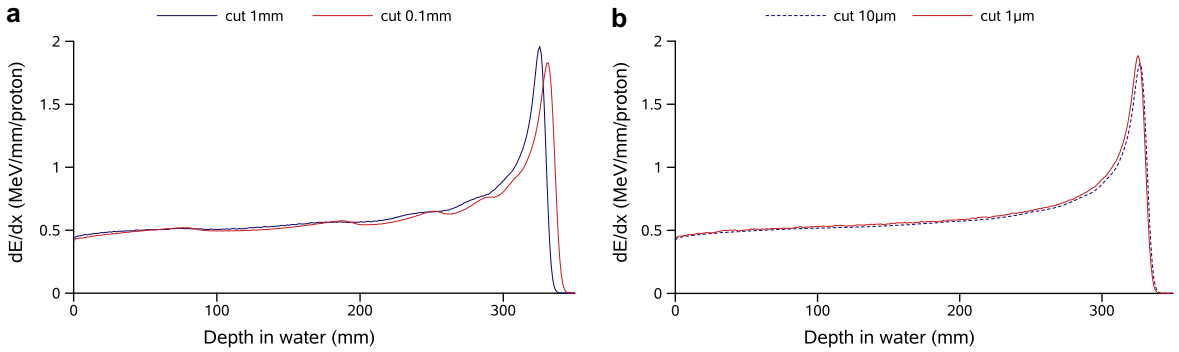

Fig. 3. Influence of the range cut threshold and hence of the step size on dose computing of 230 MeV protons in water. When a sufficiently low range cut is used, the proton range becomes stable and the dose fluctuations negligible. Influence of high range cuts is presented in (a) and low range cut in (b).

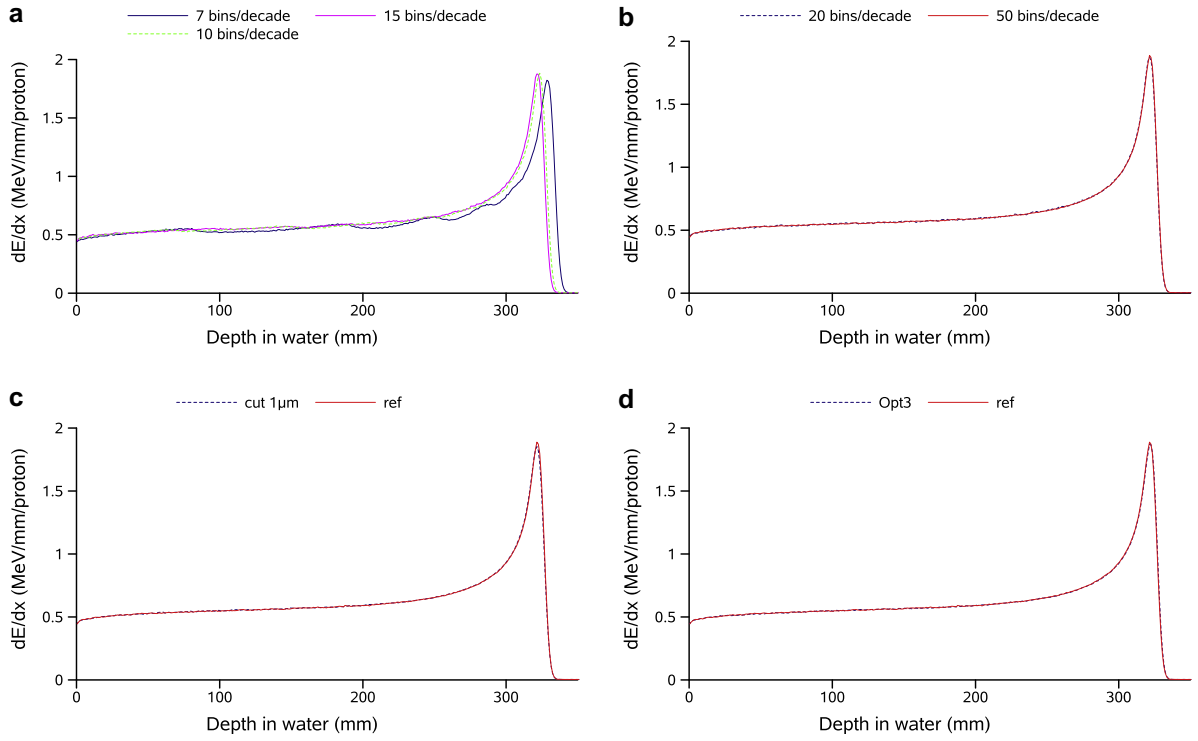

Fig. 4. (a,b) The influence of the binning parameters on dose computing with a range cut of 0.1 mm and no step limitation. When a sufficient number of bins is used, the proton range becomes stable and the dose fluctuations negligible. The influence of a 1 µm range cut (c) and GEANT4 Opt3 (d) on a simulation using 50 bins/decade is also presented.

ade simulation was considered as the reference. We simulated 3×10^5 protons, leading to a statistical uncertainty of about 0.5% from the water tank entrance up to the Bragg-peak distal fall-off. Above 15 bins/decade, the fluctuations became irrelevant, indicating that the 20 bins/decade resolution recommended by the GEANT4 Electromagnetic Standard working group is sufficient. The number of bins increased slightly the initialization time, but this was negligible even with a large number of materials (the initialization time was, respectively, 3 and 3.5 min with 7 and 20 bins/decade, for 1000 materials).

Additionally, the influence of the previously studied parameters (range cut and step size) was assessed by comparing dose deposits in the reference simulation described above and in the same simulation with a 1 µm range cut (Fig. 4(c)). No significant difference was observed. Finally, we checked the influence of the Opt3 (Fig. 4(d)). Results are summarized in Table 2.

If only a few bins are used, the tables do not accurately describe EM processes. Hence, the interpolated cross-sections are no longer constant, leading to incorrect step and continuous energy loss sampling. When limiting the step, the dose sampling along the ion track is more frequent. When a sufficient number of bins is used, the proton range and dose fluctuations are independent of the range cut and step parameters. Consequently, the range cut parameter can be used as intended, i.e. to define the accuracy of the electronic dose distribution along the ion track. For safety, it is suggested to set the range cut and maximum allowed step equal or lower than the voxel size, around 1 mm for clinical applications. The Opt3 parameters-list did not modify the results, however, the simulation was performed using a simple homogeneous geometry and both the stepping function and stepping algorithm may play a role in heterogeneous and voxelized media like patient CT data.

3.3. Efficiency-based parameter selection

Regarding the previous investigations and in the context of the clinical implementation of dose calculation, simulation efficiencies were compared between the following four simulation settings:

1. 50 bins/decade, range cut and maximum allowed step at 1 mm.
2. 50 bins/decade, range cut and maximum allowed step at 0.1 mm.
3. 50 bins/decade, range cut at 1 µm.
4. 50 bins/decade, range cut and maximum allowed step at 1 mm, Opt3.

The simulation efficiency (η) was calculated using Eq. (6), as defined in [21], taking into account the simulation time (T) and the simulation statistical uncertainty which was calculated using Eq. (2) from [22] for each dosel (dose scoring voxel [23]). The simulation statistical uncertainty (σ) was defined as the mean uncertainty of all dosels between the entrance and the proton range.

Table 2
Influence of the number of bins used to initialize the pre-calculated EM tables on dose computation and proton range. Above 15 bins/decade, simulations lie within 0.3 mm in range and 0.7% of ϵ_{80} deviations with the reference. The use of a 1 µm range cut and Opt3 did not affect the simulations.

Bins/decade	7	10	15	20	20 (Opt3)	50 (range cut 1 µm)	50 (ref)
ϵ_{80} (%)	4.8	1.7	0.7	0.7	0.5	0.5	–
Range (mm)	331.9	326.6	325.1	324.8	325.2	324.7	325.0

$$\eta = \frac{1}{\sigma^2 \times T} \tag{6}$$

Simulations were performed on a single 1.66 GHz CPU. Results are summarized in Table 3.

Settings (i) and (iv) had a comparable efficiency, while settings (ii) and (iii) were about 7 and 430 times lower, respectively. In settings (iv), Opt3 parameters were added to settings (i) and could only increase the simulation accuracy. Therefore, settings (iv) were selected as the reference parameters-list, in order to perform robust and fast simulations.

3.4. Ionization potential of water

The proton range depends mainly on the mean ionization potential (I) of the medium. The I value of water is a subject of growing interest and values between 67.2 and 85 eV are reported in Table 1 from Soltani-Nabipour et al. [24]. A recent study has also evidenced the uncertainty related to the I values of human tissues, stating that this could lead to the use of "sub-centimeter" clinical margins [25]. When the ionization potential of a medium is not known, Bragg's additivity rule [26] is used to compute it, by weighting the I values of the different constituents. In GEANT4, the ionization potential is calculated following Bragg's additivity rule by default for all user-defined media and is 70.9 eV for water. However, the user has the possibility of changing this value. We tested different values of I: 70.9, 75 and 80 eV, which moved the proton range, respectively, to 324.9, 329.2 and 330.8 mm, while the CSDA range given by NIST is 329.4 mm. Based on these results, we set the ionization potential of water to 75 eV, which is the value recommended by ICRU reports 37 and 49 [27,28]. This value was also used in MCNPX and PHITS codes.

Table 3
Simulation efficiency for four different settings.

Simulation index	i	ii	iii	iv
Statistical uncertainty (%)	1.3	1.2	1.2	1.2
Time (s)	1.4×10^2	1.2×10^3	5.4×10^4	1.5×10^2
Efficiency	4.2×10^1	5.9	1×10^{-1}	4.3×10^1

4. GEANT4 comparison with PHITS and MCNPX

Simulation time, depth-dose profiles and transverse profiles at 10, 30 and 32 cm depth simulated with GEANT4, were compared to PHITS and MCNPX for a 230 MeV proton beam, using a circular Gaussian spot of 3 mm sigma. Furthermore, we assessed the impact of the MS algorithm on the lateral dose spreading compared to the SS algorithm implemented in GEANT4. Depth-dose profiles were integrated along the z-axis with a 1 mm step and transverse profiles were scored in dosels of $2 \times 2 \times 1$ mm^3, in x, y and z (the beam direction), respectively. Default parameters were used for PHITS and MCNPX, using a MS model and the ATIMA cross-section database for PHITS. A summary of the relevant simulation parameters used for all three MC codes is given in Table 4. Transverse profiles are presented in absolute dose (Fig. 5(b)).

As regards depth-dose profiles, MCNPX and PHITS are in close agreement. Differences in the plateau and in the Bragg-peak regions compared to GEANT4 may be explained by different HAD and EM models. A detailed investigation of these differences is out of the scope of this paper, but it is worthwhile to note that the integral energy deposited by a 230 MeV mono-energetic proton beam between 0 and 40 cm is on average 215.5 MeV/proton with GEANT4, 204.7 MeV/proton with PHITS and 205.6 MeV/proton with MCNPX. The integral dose deposited by GEANT4 is 5.3% higher than PHITS and 4.8% higher than MCNPX.

In the transverse profiles one can observe differences in the maximum dose deposited in the profile centers and differences in the profile FWHM. The maximum dose of a profile calculated at a depth d depends on both the integral dose deposited at depth d (Fig. 5(a)) and on the lateral dose spreading. Simulations performed without the proton MS process yield almost no beam spreading, suggesting that proton scattering is mainly due to the MS process, even if HAD collisions may affect the profiles. Thus, the profile FWHM value is well representative of the multiple Coulomb scattering process. Regarding transverse profile FWHM, the proton beam spreading with depth in GEANT4 is narrower than in MCNPX and PHITS. Two recent studies presented a significative overestimation of the MCNPX MS algorithm compared to measurements [29,30]. Differences up to 34% in polystyrene and up to 15% in bone were reported in [29]. In [30], a modified MS algorithm is proposed to improve the accuracy of MCNPX. Dose spreading was

Table 4
This table summaries the physical, geometrical and chemical parameters used for MC calculations using GATE, PHITS and MCNPX.

Beam description		Phantom description		Dosel dimensions (x, y, z)	
E_0	230 MeV	Dimensions	$40 \times 40 \times 40$ cm^3	Depth-Dose	$400 \times 400 \times 1$ mm^3
σ_E	0 MeV	Composition	H_2O	Profiles	$2 \times 2 \times 1$ mm^3
$\sigma_{x,y}$	3 mm	I_{Water}	75 eV		

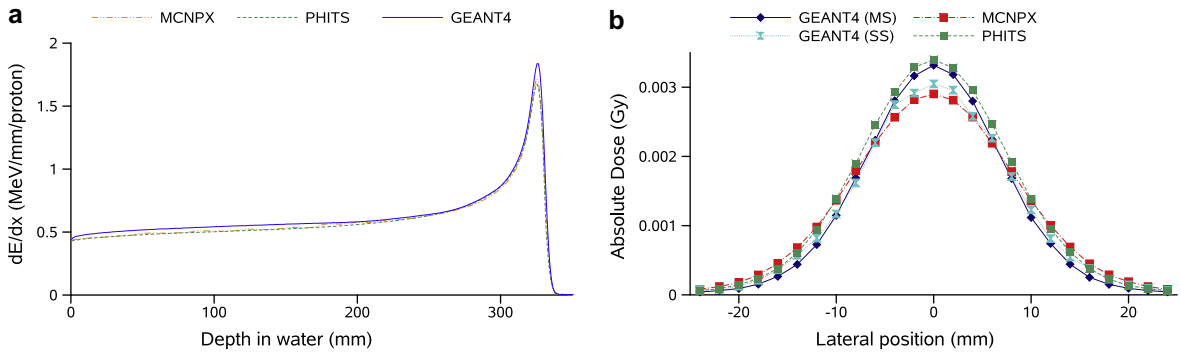

Fig. 5. Comparison of depth-dose and transverse profiles at 32 cm depth using GEANT4, MCNPX and PHITS, for a 230 MeV proton beam in water.

Table 5
Comparison of the transverse profile spreading (σ) at 10, 30 and 32 cm depth for a 230 MeV proton beam in water using the GEANT4 MS algorithm, GEANT4 SS algorithm, MCNPX, PHITS and an analytical model (Szymanowski). The uncertainty on the σ values was estimated 0.15 mm using ROOT. GEANT4 beam spreading is significantly lower than in MCNPX, PHITS and Szymanowski's model, even if it gets close to the PHITS results using the SS algorithm. MCNPX shows the widest beam spreading.

	GEANT4 (MS)	GEANT4 (SS)	MCNPX	PHITS	Szymanowski
$\sigma_{10\,cm}$ (mm)	3.1	3.2	3.1	3.4	3.2
$\sigma_{30\,cm}$ (mm)	6.2	6.8	7.3	6.8	7.1
$\sigma_{32\,cm}$ (mm)	6.9	7.5	8.1	7.5	7.8

also estimated due to an analytical formula based on measurements using Eq. (4) from [31]. Significant differences in terms of dose spreading were observed between MS and SS models of GEANT4 (8% difference in FWHM). It is noteworthy that MS algorithms should reproduce the detailed simulation results obtained with SS models. In the case of GEANT4 MS and SS models comparison, one can directly observe the overall profile difference (Fig. 5(b)), which is specific to the Coulomb scattering model selected.

Results are presented in Table 5. From this table, it seems that GEANT4 SS and PHITS MS models are in close agreement, while the dose level difference observed in Fig. 5(b) may be due to different EM and HAD modelization.

The comparisons between the different MC codes and Szymanowski's analytical model showed inconsistencies, with up to 15% difference (2.8 mm in FWHM) in the lateral dose spreading simulated with GEANT4 and with MCNPX, at 32 cm depth in water. Using a SS instead of a MS model increases the number of steps and the simulation time by three orders of magnitude (330 steps per incident proton were recorded using the MS model and more than 700×10^3 with the SS). As the computation of the spatial displacement is not part of the MS theories, each MC code has to develop its own algorithm [13], which may explain part of the discrepancies. Our first suggestion is that the proton MS process used in GEANT4.9.2 should be revised.

Regarding computation time, MCNPX and PHITS proton rates were estimated to 127 and 29 protons s^{-1}, respectively, on a single 3.06 GHz CPU using detailed simulation settings. On a comparable machine with a 2.33 GHz CPU, the GATE/GEANT4 proton rate was estimated to 263 protons s^{-1} using optimized settings. These simulation times have only an indicative purpose, since the simulations were performed on different machines, using different MC parameters.

Table 6
Pristine Bragg peak measurements for five energies. The settings at the nozzle exit (R_{Noz} and E_{Noz}) were estimated from the nozzle entrance parameters (R_{ESS} and E_{ESS}) and then measured in water (measured ranges). At the time of the measurements, the nozzle energy was not yet calibrated. This explains the discrepancies between set ranges and measured ranges.

R_{ESS} (g/cm^2)	E_{ESS} (MeV)	R_{Noz} (g/cm^2)	E_{Noz} (MeV)	Measured ranges (cm)
7.72	99.95	7.55	98.71	7.78
13.50	137.72	13.33	136.21	13.59
19.50	169.48	19.33	168.63	19.55
26.50	202.51	26.33	201.75	26.44
32.54	228.35	32.37	227.65	32.50

5. Experimental measurements

Measurements were performed in Essen, Germany, with the new IBA Pencil Beam Scanning (PBS) dedicated nozzle mounted on a rotating gantry. This nozzle allows for delivering circular spots of a few millimeters in diameter at the treatment isocenter. The Nozzle water Equivalent Thickness (NET) was estimated to 1.7 mm. The Water Equivalent Thickness (WET) of the different media within the nozzle were estimated using Eq. (7):

$$\mathrm{WET}_m = L \times \frac{\rho_m}{\rho_w} \times \frac{S_m}{S_w} \tag{7}$$

where the index m stand for medium and w for water. S and ρ are the mass stopping powers (in MeV cm^2 g^{-1}) and densities (in g cm^{-3}), respectively. WET_m is the medium WET (in cm) and L its thickness (in cm).

The Energy Selection System (ESS) is designed to provide one given beam of range rmR_{ESS} and energy E_{ESS} at the nozzle entrance. The corresponding range R_{Noz} and energy E_{Noz} at the nozzle output were therefore obtained by subtracting the NET. The R_{ESS} and R_{Noz} given correspond to ranges in water. Range to energy conversion was determined with a fit from the NIST PSTAR database [18]. The ESS was tuned to achieve energy spreads lower than 1% of the mean energies. Beam optic simulations suggest an increase in energy spread when decreasing the mean energy of the beam.

5.1. Reference pristine Bragg peak in water

Reference pristine Bragg peaks were measured in a $60 \times 60 \times 60$ cm^3 water phantom (Blue Phantom®, IBA-Dosimetry) for five energies, as presented in Table 6. Two large Bragg-peak

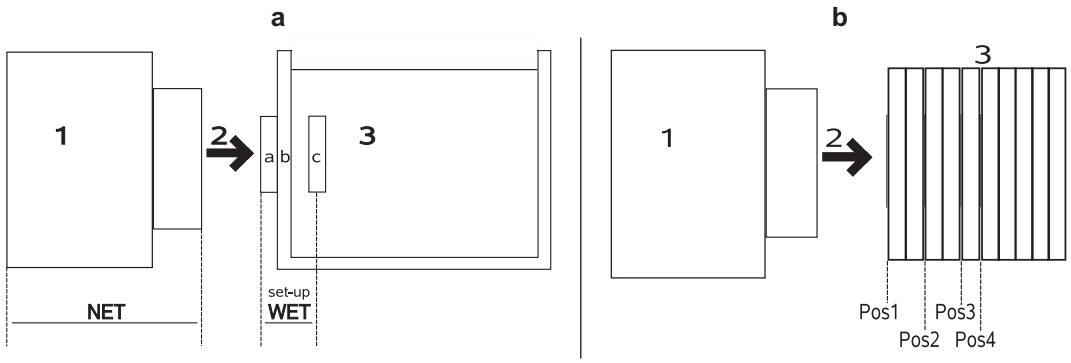

Fig. 6. Illustration of the measurement set-up of depth-dose profiles in water (A) and transverse profiles in PMMA (B). (A) The nozzle (1), the proton beam direction (2) and the water phantom (3), with the reference Bragg-peak chamber (a), the sensitive Bragg-peak chamber (c) and the phantom entrance wall (b). (B) The transverse profile set-up of the 98.71 MeV proton beam, with four radiochromic films (in blue) inserted between the PMMA slabs (3). (For interpretation of the references to colour in this figure legend, the reader is referred to the web version of this article.)

Table 7
Positions of the transverse profiles measured with EBT radiochromic films inserted in a PMMA phantom. Four films were used at the lowest and medium energies and five at the highest energy.

E_{Noz} (MeV)	R_{Noz} (g/cm^2)	Range in PMMA (cm)	Pos 1 (mm)	Pos 2 (mm)	Pos 3 (mm)	Pos 4 (mm)	Pos 5 (mm)
98.71	7.55	6.34	0	19	49	59	–
153.01	16.33	13.72	0	50	99	128	–
210.56	28.33	23.81	0	88	186	216	226

chambers (PTW type 34070) with a 10.5 cm^3 sensitive volume were used, so that the proton beams were always fully integrated within the sensitive volume of the chamber (Fig. 6(a)). The first chamber was placed at the phantom entrance and used as a reference chamber to eliminate beam fluctuations. The second chamber was placed in the phantom and moved along the z-axis with a 1 mm increment. Measured depth-dose profiles were shifted by 44.1 mm to account for the total set-up WET to the effective measurement point. The uncertainty on the measured energy deposited depends mainly on the signal level and was estimated to be about 1%.

5.2. Reference transverse profiles in PMMA

Reference transverse profiles were measured with ISP self-developing EBT Gafchromic® films inserted between uncalibrated PMMA slabs of 1 cm thickness (Fig. 6(b)) and 1.19 g cm^{-3} density. The exact positions of the films between the slabs were recorded. Transverse profiles were measured for three different energies, with four or five films inserted between the slabs as summarized in Table 7. The film optical densities (OD) were recorded using a Vidar VXR-16 DosimetryPRO Film Digitizer (Vidar Corporation, Herndon, Virginia) at the Centre Lèon Berard (Lyon, France). For each film, the mean OD of a non-irradiated film, considered as the background, was subtracted before normalization to the maximum OD. Transverse profiles were measured with a grid resolution of 1×1 mm^2, to mimick the simulated matrix of dosels. At the time of the measurements, only a preliminary version of the PBS system was available and the monitor units were not yet available. Therefore, it was not possible to perform a calibration curve between the film OD and doses. These preliminary measurements were used only qualitatively to illustrate the beam widening increase with depth.

6. GEANT4 comparison with measurements

6.1. Depth-dose in water

The evaluation of depth-dose profile simulations was based on three criteria: the proton range, the peak dose deviation and the mean point-to-point dose deviation. Simulated and measured depth-dose profiles were normalized to the integral dose deposited. There was a discrepancy between measured ranges and system ranges, because the nozzle had not been yet properly calibrated at the time of the measurements: the energies were slightly higher than the set values, leading to measured ranges increased by 1.1–2.6 mm (Table 6). To further assess the dose deposited, we shifted the measurements to compensate for the range difference with the simulations. Then, we adjusted the energy spread of the incident beams in the simulation for the five energies to match the measurements as closely as possible. The tuning stage of the energy spread was done with an energy step of 0.05–0.1% of the mean energy. The energy spread was adjusted according to two criteria: the peak dose deviation and the mean point-to-point dose deviation (ϵ_{80}) calculated using Eq. (5). Results obtained at the lowest and highest energies are presented in Fig. 7.

We simulated 10^5 protons. Lower peak dose deviations were associated with lower mean point-to-point dose deviations, as presented for $E_{Noz} = 168.63$ MeV in Fig. 8. For absolute range comparison, the simulated range accuracy depends on the nozzle WET

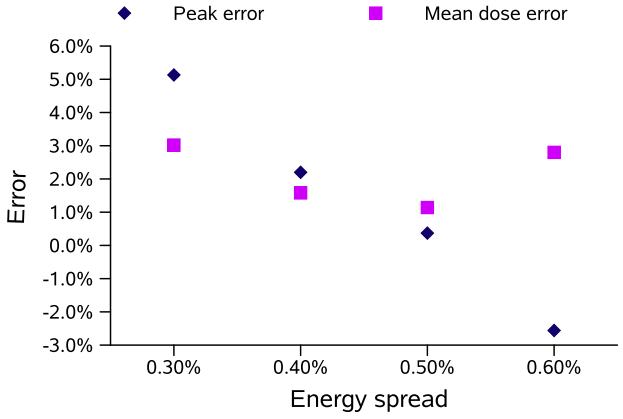

Fig. 8. Tuning of the 168.63 MeV proton beam, by adjusting the energy spread of the simulation. The lowest peak deviation and ϵ_{80} deviation ("mean dose error") correspond to a sigma energy spread of 0.5% of the mean energy of initial beam.

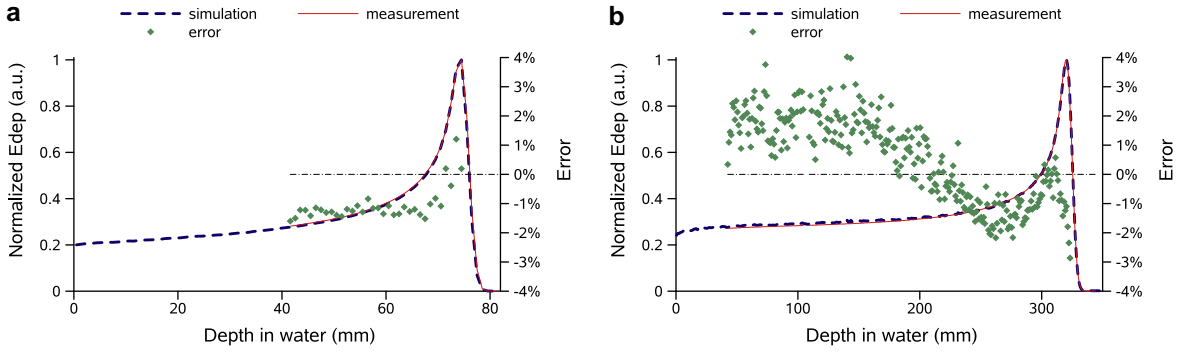

Fig. 7. Comparison between measured and simulated depth-dose profiles in water for the highest and lowest energies, 227.65 MeV (b) and 98.71 MeV (a). The left and right axes correspond to normalized doses and point-to-point deviations, respectively.

Table 8
Assessment of depth-dose profiles in water, in terms of peak dose deviation (ϵ_{peak}), mean point-to-point dose deviation (ϵ_{80}) and range accuracy.The energy spread (σ_E in %) adjusted in the simulations increased with decreasing energy within 0.1–0.6%, as expected from the system (ESS).

R_{Noz} (g/cm^2)	E_{Noz} (MeV)	σ_E simulation (%)	ϵ_{80} (%)	ϵ_{peak} (%)	R_{simu} (cm)
32.37	227.65	0.10	1.1	1.1	32.35
26.33	201.75	0.30	0.9	0.4	26.33
19.33	168.63	0.50	0.8	0.4	19.33
13.33	136.21	0.55	1.2	−0.8	13.31
7.55	98.71	0.60	1.2	0.4	7.52

estimation, the ionization potential uncertainty of the different element crossed (nozzle component, water phantom) and the scoring resolution. In this study, we did not simulate the nozzle, but we compared simulated ranges in a water phantom to NIST values. The ionizaton potential was used as a "free parameter", as discussed in Section 3.4. Thus, the simulated range accuracy depends mainly on the scoring grid resolution. As millimetric dosels were used along the beam axis, we assumed that a 0.5 mm range accuracy could be achieved, or better. In Fig. 7(a), one can observe that the resolution of 1 mm for calculations and measurements was too small, because the peak was not correctly covered. At higher energy however, the peak width was larger and better covered, hence, one could expect a better range estimation. Simulated ranges laid within 0.3 mm of set ranges. Peak dose deviations and mean point-to-point dose deviations were about 1%. Results are summarized in Table 8.

The dose statistical uncertainty of our MC calculation was about 0.8% in the plateau region and about 0.4% in the Bragg-peak region. Consequently, these results were in good agreement with the measurements.

6.2. Transverse dose profiles in PMMA

The simulation of the lateral dose spreading of individual pencil beams was assessed against measurements for three energies (98.71, 153.01 and 210.56 MeV). Transverse profiles were measured at several depths in a PMMA phantom using radiochromic films, as presented in Fig. 6(b). The beam energy parameters were determined from the previous depth-dose profile simulations.

The dose response mechanism of radiochromic films is not linear with dose and depends on the particle's Linear Energy Transfer (LET) [32,33]. Radiochromic films show a significant under-response in the Bragg-peak region, because of quenching effects due to high-LET particles [32,33]. The radiochromic film's dose response has been modeled following a logarithmic relation in [32], as shown in Eq. (8):

$$OD^{net}(D_{eff}) = \log(a' \cdot D_{eff} + 1) \tag{8}$$

with a' the film's response parameter, $OD^{net}(D_{eff})$ the net optical density after irradiation with an effective dose D_{eff}, which depends on the particle LET and dose deposit D. For low LET, $D_{eff} \simeq D$. As the LET increases, D_{eff} becomes lower than D, illustrating the film's under-response.

The particle LET increases as its remaining range decreases with penetration in water. Hence, for depth-dose profile measurements, the film's response dependence on LET has to be accounted for. Since our measurements were transverse to the beam direction, the LET lateral variations were neglected in first approximation. Additional tests using MC showed that, as the depth of calculation increased, the mean LET value was slightly higher on the side of the transverse profiles compared to the center. This suggests a lower dose response on the side of the transverse profiles compared to the center (due to quenching effect), which may lead to an underestimation of the FWHM in depth. However, it has been stated in [34], that radiographic films and diodes, which are detectors that are also sensitive to the energy spectrum of protons, can be safely used to measure distributions perpendicular to the proton beam direction.

We compared the film's OD FWHM ($FWHM_{OD}$) increase to the simulated transverse dose profile FWHM ($FWHM_{simu}$) increase with depth. A Gaussian fit on the radiochromic film OD measured at the beam entrance was performed using the ROOT software [35] for the three energies. The spot FWHM in the x- and y-directions were then used as input parameters in the simulations, so that $FWHM_{simu} = FWHM_{OD}$ at the phantom entrance. The measured spot widths (sigma in OD) were between 3 and 6 mm depending on the energy. The uncertainty of radiochromic film measurements was estimated to 5% for MD-55-2 films in [36]. The FWHM uncertainty of the fit was estimated to be 0.1 mm.

Assuming $FWHM_{dose}$ the true dose FWHM, it follows from the logarithmic relationship between OD and dose (Eq. (8)), that for a fixed $FWHM_{dose}$, the $FWHM_{OD}$ decreases while the dose decreases (Fig. 9(b)). Hence, the true dose spreading increase with depth should be even higher than the "OD spreading" increase with depth, because the dose at the beam axis decreases with depth (contrary to the integral dose). This is illustrated in Fig. 9.

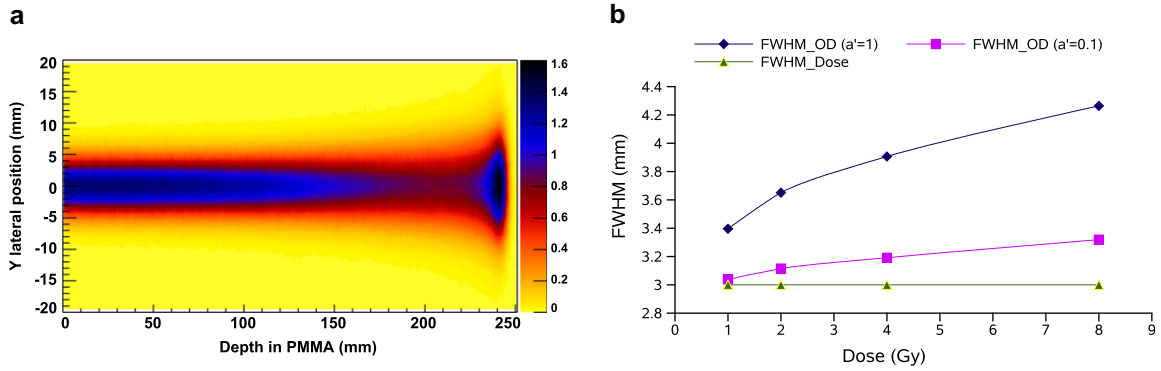

Fig. 9. (a) Simulated dose spreading with depth in PMMA of a 211 MeV proton beam with a circular spot of 3 mm sigma. While the integral depth-dose increases continuously with depth, the depth-dose at the beam axis decreases with depth with a factor about 2 between the entrance and the Bragg peak and increases again within the last 2 cm. (b) Illustration of the $FWHM_{OD}$ increase with increasing dose, compared to a constant $FWHM_{dose}$ of 3 mm, with a maximum dose varying between 1 and 8 Gy, for two different film parameters: a′ = 1 and a ′ = 0.1. This comparison was only theoretical (without measurements), using the film's dose response model presented previously (Eq. (8)).

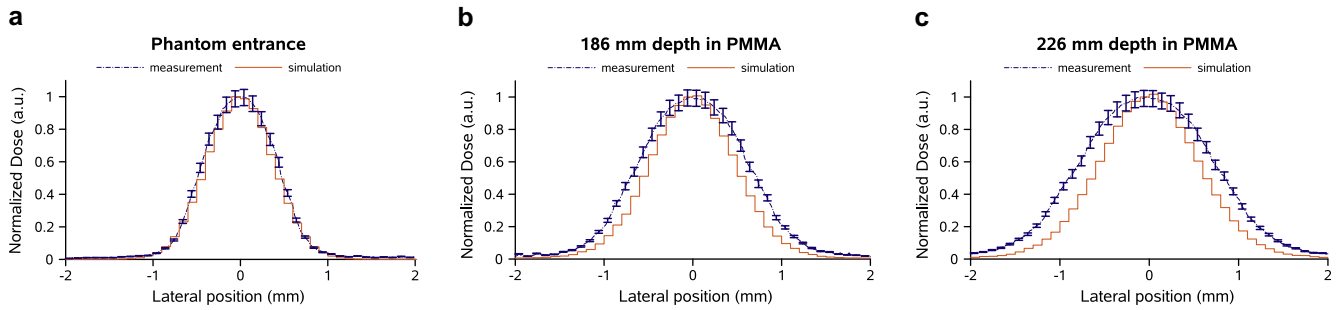

Fig. 10. Comparison between simulated transverse dose profiles and measured transverse OD profiles in PMMA, for a 210.56 MeV proton beam at three depths: 0, 186 and 226 mm. It shows that the beam spreading with depth is not sufficiently accounted for in the simulation. Error bars are printed for the measurements and correspond to the measurement uncertainty of 5% [36]. For the simulations, error bars are very low, due to the low statistical uncertainty, thus they are not printed.

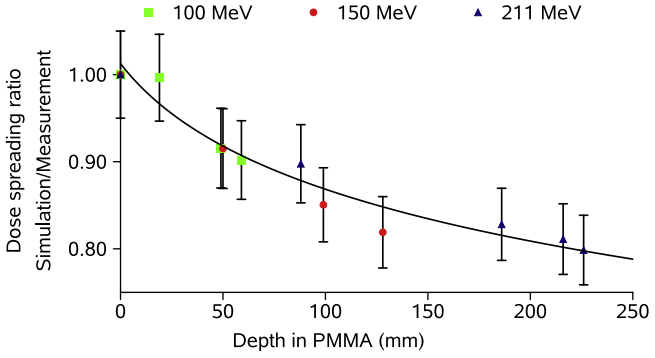

Fig. 11. This figure illustrates the lack of lateral dose spreading with depth compared to measurements in PMMA, using the GEANT4 MS model. Comparisons are shown at three energies (210.56, 153.01, 98.71 MeV). The black line shows the general trend of the transverse dose spreading underestimation with depth. Error bars are also printed.

Results obtained using GEANT4 for x profiles with $E_{Noz} =$ 210.56 MeV at three different depths are presented in Fig. 10. Similar results were obtained for the two other energies (153.01 and 98.71 MeV). The $\frac{\mathrm{FWHM}_{simu}}{\mathrm{FWHM}_{OD}}$ ratio at different depths for the three energies is presented in Fig. 11 and illustrates the lack of dose spreading with depth of the GEANT4 MC code compared to measurements. It is important to notice, that the previous discussions about the film LET and dose response dependences suggested that the qualitative measurements presented, also underestimate the true lateral dose spreading with depth. This study corroborates the fact that the MS model implemented in GEANT4.9.2 release underestimates the lateral dose spreading with depth, even though further comparisons with quantitative measurements are required to fix the dose spreading accuracy achievable by MC simulation with GEANT4.

7. Discussion and conclusion

The objective of this study on proton PBS simulations was to get a better understanding of the GEANT4 settings. Two dominant simulation parameters are the maximum step size and the range cut, which should be defined in accordance to the voxel size. Another key parameter is the binning of the EM tables, which needs to be set to a value >15 bins/decade to ensure accurate interactions, independent of the range cut and maximum allowed step values. An optimized parameters-list has been proposed in order to perform robust and efficient simulations, that are competitive in term of simulation time with other MC codes like MCNPX and PHITS. A reference physics-list for proton therapy has been presented, using the EM standard package combined with the precompound model for inelastic HAD collisions. It is noteworthy that the absolute dose deposited for a 230 MeV proton beam simulated with GEANT4 was about 5% higher than with PHITS and MCNPX.

When comparing simulated and measured ranges, not only the approximated WET of the nozzle accounts for range differences, but the ionization potential uncertainty of the different media influences the range as well. Therefore, it is necessary to know the correct WET of the nozzle to make any conclusion on absolute ranges. As the beam energy of the nozzle was not calibrated, we did not perform absolute range comparison. We used NIST values as a reference instead. The ionization potential of water was set to 75 eV, in accordance with ICRU reports 37 and 49, because it was found to best reproduce NIST CSDA ranges for 5 energies between 100 and 230 MeV (within 0.3 mm). Depth-dose profile simulations were in satisfactory agreement with reference measurements performed in water. Peak deviations were less than 1.1% and mean point-to-point deviations (ϵ_{80}) were about 1%. Dose differences between simulations and measurements are within the measurement and calculation uncertainties (about 1%). Range differences compared to NIST are within the simulation uncertainties (about 0.5 mm).

Inconsistencies were pointed out for transverse profile simulations using different MC codes, with up to 15% difference in dose spreading between GEANT4 and MCNPX at 32 cm depth in water. Transverse dose profile simulation issues using GEANT4 were attributed to the MS algorithm, which was not able to reproduce the SS dose spreading with depth. Further comparisons against measurements in PMMA corroborated these results and showed that the lateral dose spreading with depth is not sufficiently accounted for in GEANT4. Radiochromic films have a very high spatial resolution, which is contrary to their associated reading uncertainty and dose response dependence. Therefore, radiochromic films may be not the most suited tool for the validation of transverse profile simulations. The significantly larger dose spreading simulated with MCNPX may suggest a better modeling of the MS process, but this conclusion is contrary to other investigations [29,30], which demonstrate that MCNPX overestimates the scattering with respect to measurements. As the PHITS MS model was in good agreement with the GEANT4 SS model, it could be a good candidate. However, the investigations performed in this study do not allow to firmly conclude on which code to prefer.

The MS algorithm accuracy is currently the limiting factor for PBS simulations, since the dose spreading of each single beam is very important for patient dose calculation. Improvements of the MS algorithm are expected with the new GEANT4.9.3 release, which is being evaluated. Investigations using quantitative measurements are necessary to fully estimate the lateral dose spreading accuracy achievable by MC simulation. Further studies investigating the effects of patient heterogeneities, using a MC

pencil beam model of the new IBA PBS dedicated system and related TPS comparisons will follow.

Acknowledgments

This work was conducted in a collaboration between IBA and the Creatis laboratory. The research leading to these results has received funding from the [European Community's] Seventh Framework Programme [FP7/2007-2013] under grant agreement no. 215840-2. We also acknowledge the GEANT4 collaboration, especially Vladimir Ivantchenko for fruitful discussions.

References

[1] U. Amaldi, G. Kraft, Radiotherapy with beams of carbon ions, Rep. Prog. Phys. 68 (2005) 1861–1882.
[2] H. Paganetti, H. Jiang, K. Parodi, R. Slopsema, M. Engelsman, Clinical implementation of full Monte Carlo dose calculation in proton beam therapy, Phys. Med. Biol. 53 (2008) 4825–4853.
[3] S. Jan, G. Santin, D. Strul, S. Staelens, K. Assié, D. Autret, S. Avner, R. Barbier, M. Bardiès, P.M. Bloomfield, D. Brasse, V. Breton, P. Bruyndonckx, I. Buvat, A.F. Chatziioannou, Y. Choi, Y.H. Chung, C. Comtat, D. Donnarieix, L. Ferrer, S.J. Glick, C.J. Groiselle, D. Guez, P.-F. Honore, S. Kerhoas-Cavata, A.S. Kirov, V. Kohli, M. Koole, M. Krieguer, D.J. van der Laan, F. Lamare, G. Largeron, C. Lartizien, D. Lazaro, M.C. Maas, L. Maigne, F. Mayet, F. Melot, C. Merheb, E. Pennacchio, J. Perez, U. Pietrzyk, F.R. Rannou, M. Rey, D.R. Schaart, C.R. Schmidtlein, L. Simon, T.Y. Song, J.-M. Vieira, D. Visvikis, R.V. de Walle, E. Wieërs, C. Morel, Gate: a simulation toolkit for pet and spect, Phys. Med. Biol. 49 (2004) 4543.
[4] J. Seco, H. Jiang, D. Herrup, H. Kooy, H. Paganetti, A Monte Carlo tool for combined photon and proton treatment planning verification, J. Phys.: Conf. Series 74 (2007) 021014.
[5] N. Zahra, T. Frisson, L. Grevillot, P. Lautesse, D. Sarrut, Influence of Geant4 parameters on dose distribution and computation time for carbon ion therapy simulation, Phys. Med. (2010), doi:10.1016/j.emp.2009.12.001.
[6] MCNPXTM User's Manual Version 2.5.0, Los Alamos National Laboratory Report LA-CP-05-0369, 2005.
[7] K. Niita, T. Sato, H. Iwase, H. Nose, H. Nakashima, L. Sihver, PHITS – a particle and heavy ion transport code system, Space Radiation Transport, Shielding, and Risk Assessment Models, 2006.
[8] Geant4 Electromagnetic Standard Working Group, 2009.
[9] C.Z. Jarlskog, H. Paganetti, Physics settings for using the Geant4 toolkit in proton therapy, IEEE 55 (2008) 1018–1024.
[10] J. Wellisch, Geant4 hadronic physics status and validation for large HEP detectors, Computing in High Energy and Nuclear Physics, La Jolla, California, March 24–28, 2003.
[11] L. Sihver, D. Matthiä, T. Koi, D. Mancusi, Dose calculations at high altitudes and in deep space with GEANT4 using BIC and JQMD models for nucleus–nucleus reactions, New J. Phys. (2008).
[12] J. Apostolakis, M. Asai, A. Bogdanov, H. Burkhardt, G. Cosmo, S. Elles, G. Folger, V. Grichine, P. Gumplinger, A. Heikkinen, I. Hrivnacova, V. Ivantchenko, J. Jacquemier, T. Koi, R. Kokoulin, M. Kossov, H. Kurashige, I. McLaren, O. Link, M. Maire, W. Pokorski, T. Sasaki, N. Starkov, L. Urban, D. Wright, Geometry and physics of the Geant4 toolkit for high and medium energy applications, Radiat. Phys. Chem. 78 (2009) 859–873 (Workshop on Use of Monte Carlo Techniques for Design and Analysis of Radiation Detectors).
[13] Geant4-Collaboration, Physics Reference Manual for Geant4, CERN, 2009.
[14] S.W. Peterson, J. Polf, M. Bues, G. Ciangaru, L. Archambault, S. Beddar, A. Smith, Experimental validation of a Monte Carlo proton therapy nozzle model incorporating magnetically steered protons, Phys. Med. Biol. 54 (2009) 3217–3229.
[15] J.C. Polf, S. Peterson, M. McCleskey, B.T. Roeder, A. Spiridon, S. Beddar, L. Trache, Measurement and calculation of characteristic prompt gamma ray spectra emitted during proton irradiation, Phys. Med. Biol. 54 (2009) N519–N527.
[16] N. Kanematsu, Alternative scattering power for gaussian beam model of heavy charged particles, Nucl. Instr. Methods Phys. Res. Sect. B: Beam Interact. Mater. Atoms 266 (2008) 5056–5062.
[17] B. Gottschalk, On the scattering power of radiotherapy protons, Med. Phys. 37 (2010) 352–367.
[18] M. Berger, J. Coursey, M. Zucker, J. Chang, Proton Stopping Power and Ranges, Nuclear Institute of Standards and Technology, 2009. Available from: <http://physics.nist.gov/PhysRefData/Star/Text/PSTAR.html>.
[19] J.F. Ziegler, The stopping of energetic light ions in elemental matter, J. Appl. Phys.: Rev. Appl. Phys. 85 (1999) 1249–1272.
[20] S. Agostinelli et al., Geant4 – a simulation toolkit, Nucl. Instr. Methods Phys. Res. A (2003) 250–303.
[21] I.J. Chetty, B. Curran, J.E. Cygler, J.J. DeMarco, G. Ezzell, B.A. Faddegon, I. Kawrakow, P.J. Keall, H. Liu, C.M.C. Ma, D.W.O. Rogers, J. Seuntjens, D. Sheikh-Bagheri, J.V. Siebers, Report of the aapm task group no. 105: issues associated with clinical implementation of Monte Carlo-based photon and electron external beam treatment planning, Med. Phys. 34 (2007) 4818–4853.
[22] I.J. Chetty, M. Rosu, M.L. Kessler, B.A. Fraass, R.K.T. Haken, F.-M.S. Kong, D.L. McShan, Reporting and analyzing statistical uncertainties in Monte Carlo-based treatment planning, Int. J. Radiat. Oncol. Biol. Phys. 65 (2006) 1249–1259.
[23] D. Sarrut, L. Guigues, Region-oriented CT image representation for reducing computing time of Monte Carlo simulations, Med. Phys. 35 (2008) 1452–1463.
[24] J. Soltani-Nabipour, D. Sardari, G. Cata-Danil, Sensitivity of the Bragg peak curve to the average ionization potential of the stopping power, Rom. J. Phys. 54 (2008) 321–330.
[25] P. Andreo, On the clinical spatial resolution achievable with protons and heavier charged particle radiotherapy beams, Phys. Med. Biol. 54 (2009) N205–N215.
[26] W.H. Bragg, R. Kleeman, On the α particles of radium, and their loss of range in passing through various atoms and molecules, Philos. Mag. 10 (1905) 318–340.
[27] Bethesda, MD: ICRU Report 37: Stopping Powers for Electrons and Positrons, 1984.
[28] Bethesda, MD: ICRU Report 49: Stopping Powers and Ranges for Protons and Alpha Particles, 1993.
[29] C.J. Mertens, M.F. Moyers, S.A. Walker, J. Tweed, Proton lateral broadening distribution comparisons between GRNTRN, MCNPX, and laboratory beam measurements, Adv. Space Res. 45 (2010) 884–891 (Life Sci. Space).
[30] A. Stankovskiy, S. Kerhoas-Cavata, R. Ferrand, C. Nauraye, L. Demarzi, Monte Carlo modelling of the treatment line of the Proton Therapy Center in Orsay, Phys. Med. Biol. 54 (2009) 2377–2394.
[31] H. Szymanowski, A. Mazal, C. Nauraye, S. Biensan, R. Ferrand, M.C. Murillo, S. Caneva, G. Gaboriaud, J.C. Rosenwald, Experimental determination and verification of the parameters used in a proton pencil beam algorithm, Med. Phys. 28 (2001) 975–987.
[32] T. Frisson, N. Zahra, P. Lautesse, D. Sarrut, Monte-carlo based prediction of radiochromic film response for hadrontherapy dosimetry, Nucl. Instr. Methods Phys. Res. Sect A: Accelerat. Spectr. Detect. Assoc. Equipm. 606 (2009) 749–754.
[33] D. Kirby, S. Green, H. Palmans, R. Hugtenburg, C. Wojnecki, D. Parker, LET dependence of GafChromic films and an ion chamber in low-energy proton dosimetry, Phys. Med. Biol. 55 (2010) 417–433.
[34] Prescribing, recording, and reporting proton-beam therapy: contents, J. ICRU 7 (2007).
[35] F. Rademakers, R. Brun, Root: an object-oriented data analysis framework, Linux J. (51) (1998).
[36] Radiation Therapy Committee Task Group No. 55, Radiochromic Film Dosimetry, Technical Report, AAPM Report No. 63, 1998.